Journal of
Materials Chemistry C

Accepted Manuscript

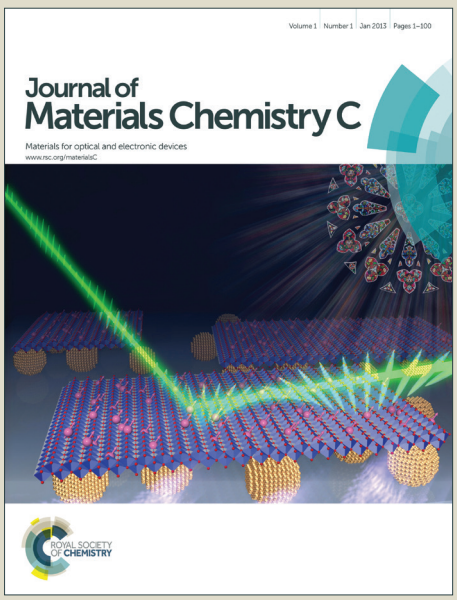

ROYAL SOCIETY OF CHEMISTRY

www.rsc.org/materialsC

Simultaneous broadband near-infrared emission and magnetic properties from single phase Ni^{2+}-doped β-Ga_2O_3 nanocrystals via mediated phase-controlled synthesis

Suiying Ye †, Yuanhao Zhang †, Huilin He, Jianrong Qiu, Guoping Dong *

State Key Laboratory of Luminescent Materials and Devices and Institute of Optical Communication Materials, South China University of Technology, Guangzhou 510640, China

Abstract: Monodisperse rice-like Ni^{2+}-doped β-Ga_2O_3 nanostructures were phase-controllably synthesized via hydrothermal route and subsequent calcination. The detailed phase, composition and morphology were characterized by X-ray diffraction (XRD), scanning electron microscope (SEM) and high resolution transmission electron microscopy (HRTEM), which showed the rice-like β-Ga_2O_3 nanostructures were assembled with nanorods with a diameter of ~50 nm along their entire length. The phase formation and transition behavior of β-Ga_2O_3 nanocrystals were investigated, and a possible crystal growth mechanism of rice-like GaOOH nanostructure was proposed. Photoluminescence (PL) spectra indicated that Ni^{2+}-doped β-Ga_2O_3 phosphors exhibit a broadband near-infrared emission (1200~1600 nm). Besides, the magnetic property was also investigated, revealing the Ni^{2+}-doped β-Ga_2O_3 nanocrystals a ferromagnetic nature. The single phase Ni^{2+}-doped β-Ga_2O_3 nanocrystals endowed with optical and magnetic bifunctional properties have promising potential application in the fields of optical communication, biological diagnosis and magnetic information storage, etc.

Keywords: gallium oxide (Ga_2O_3), phase-controlled, broadband near-infrared (NIR) emission, magnetic properties

† Equal contribution to this work.
* Author to whom correspondence should be addressed. E-mail address: dgp@scut.edu.cn

1. Introduction

In recent years, near-infrared (NIR) luminescence nanomaterials have aroused extensive attention due to their considerable promise in the fields of optical communication and bioimaging applications[1-2]. As known to all, the central wavelengths sited at 1310 nm and 1550 nm within NIR range are the second and third windows of optical communication, respectively, presenting a low optical absorption, which play an indispensable role in the advancement of the optical communication technology. It has been widely studied that nanomaterials, with Er^{3+} ions or Ni^{2+}-doped, such as Er^{3+} ions and In_2O_3 nanocrystals codoped SiO_2 films, Er^{3+}-doped SnO_2, and Ni^{2+}-doped $ZnAl_2O_4$ nanostructures, could realize a broadband NIR emission, which display a potential applications in micro/nano-broadband optical amplifiers and fibers[3-5]. What is more, NIR luminescence is also considered as a relatively harmless light for human body, owing to the contribution of its advantages of deeper light penetration, lower autofluorescence and less light scattering, making it possible to demonstrate a promising biomedical application prospect including bio-labels, medical diagnosis, and drug carriers, *etc*. In consideration of the attractive application prospects above, controllable synthesis of broadband NIR luminescence nanomaterials covering the two functional windows have attracted massive attention.

As proposed in the previous work [6-16], Gallium oxide, with a semiconductor characteristic, has been widely used in the areas of gas sensors, optoelectronic devices, luminescent materials and catalysts. Thereby, the synthesis or stabilization of it and relative oxide materials have attracted considerable attention[17-19]. It is reported that the Ga_2O_3 crystal possesses the following five crystalline forms: α-form, β-form, γ-form, δ-form and ε-form[20], and among these crystalline forms, β-Ga_2O_3 crystal, the most stable form (melt point at 1740 °C), has a monoclinic structure equipped with the O^{2-} ions in the distorted ccp arrangement and Ga^{3+} ions in the distorted tetrahedral and

octahedral sites[21-22]. While α-Ga_2O_3 crystal could generate prior to the formation of β-phase Ga_2O_3 crystal from the as-prepared precursor, crystallizing in a structure of corundum[23]. Moreover, with a wide bandgap about 4.7 eV, the β-Ga_2O_3 crystal has extended transparency to the deep ultraviolet wavelength range among transparent semiconducting oxides, and coupling with a strong absorption below 260 nm[24]. Meanwhile, the β-Ga_2O_3 has also been investigated as a excellent host material, for example, the Dy^{3+}-doped β-Ga_2O_3 phosphor has been successfully synthesized by Li et.al, showing a potential application in the photoluminescence areas and field emission display devices[25]. Generally, doping is an effective strategy to tailor the optical properties of materials, the rare earth ions have been extensively researched as the dopants in the luminescence materials, giving rise to sharp characteristic peaks with a narrow full width at half maximum (FWHM) due to the 4f orbits forbidden transition, which has not lived up to our expectations of broadband NIR luminescence. Therefore, transition metal ions, as the candidate dopants for realize a broadband NIR luminescence, have attracted considerable attention[26]. As suggested in the previous works[5,27], the Ni^{2+} ion gives a broadband NIR emission with a center around 1400 nm when occupying an octahedral site in various materials, which is attributed to both its $3d^8$ electronic configuration and strong influence on splitting of energy level caused by the electrostatic potential, owing to the contribution of neighborhood ions. Interestingly，some researchers on glass-ceramics have reported that Ga^{3+} ions possess both tetrahedral and octahedral coordination but prefer choosing the octahedral one in the β phase host lattice[28], the Ni^{2+} ions preferentially replace the Ga^{3+} ions located at octahedral sites in the β phase host lattice [29-34]. From this point of view, with the aim of obtaining a broadband NIR emission in β-Ga_2O_3 host materials, we can choose Ni^{2+} ions as the dopants to study its NIR luminescence properties. To the best knowledge of us, there are already several relative reports on broadband NIR luminescence deriving from Ni^{2+}-doped β-Ga_2O_3

nanocrystals embedded in transparent glass–ceramics[33-35], however, little efforts have been made for the controllable synthesis of the monodisperse Ni^{2+}-doped β-Ga_2O_3 nanocrystals with a broadband NIR luminescence yet.

Up to now, materials with optical-magnetic (OM) interactions are of great significance for the potential application in advanced multifunctional devices[36-39]. Hitherto, as widely implemented in research, OM interactions in materials are still confined to just the composite materials combining of two seperated pahses which contain optical and magnetic properties, respectively. For instance, magnetic-luminescence bifunctional sensor was constructed via combining luminescent $LaVO_4:Eu^{3+}$ nanocrystals with magnetic Fe_3O_4 nanoparticles[40], in addition, Fe_3O_4/ZnS:Mn equipped with these two properties was also obtained via the same method[41] and proceeded with an improvement of the properties via Fe_3O_4@$Gd_2O_3:Eu^{3+}$ core-shell structure[42]. However, it is noteworthy that OM bifunctional materials without the separation between optical and magnetic phase would be great valuable for devices in applications including high-accuracy communications, aircraft guidance, and magnetic field detection[43-44]. Thus, it gains much attention to prepare the bifunctional materials equipped with both NIR luminescence and magnetic properties in a single phase. Fortunately, relevant new progress has been witnessed in different concentration Ni^{2+} ions doped ZnO nanoparticles[45]. That is to say, Ni^{2+} ions endow not only broad NIR emission but also exhibit magnetic property. Therefore, much more extensive attention has attracted to the simultaneous broadband near-infrared emission and magnetic properties from single phase Ni^{2+}-doped nanocrystals.

In this work, monodisperse Ni^{2+}-doped β-Ga_2O_3 nanocrystals with rice-like morphology were successfully be synthesized for the first time. The crystallization process and phase transformation from the precursor GaOOH, α-Ga_2O_3 to β-Ga_2O_3 have been discussed in detail. In addition, the

morphologies of prepared samples and the possible growth formation mechanism have been detailed studied. Besides, photoluminescence (PL) properties and the magnetic property have been also investigated in detail. Based on the results above, it is believe that the novel optical-magnetic bifunctional materials have been achieved in the single phase Ni^{2+}-doped β-Ga_2O_3 nanocrystals.

2. Experimental

2.1 Materials

The raw materials are commercial gallium oxide [Ga_2O_3, 99.99%, Sinopharm Chemical Reagent Co.], nickel chloride [$NiCl_2 \cdot 6H_2O$, 99.99%, Tianjin Damao Chemical reagent Factory], Sodium dodecylbenzenesulfonate (SDBS) [$C_{18}H_{29}NaO_3S$, ≥85.0%, Yonghua Chemical Technology (Jiangsu) Co.], hydrochloric acid, aqueous ammonia and absolute alcohol. All the materials were of A.R. grade and used as received without further purification.

2.2 Synthesis

GaOOH precursor and α-Ga_2O_3, β-Ga_2O_3 nanocrystals with 0%, 1%, 3%, 5% Ni^{2+} doping (in mol) were synthesized via a hydrothermal route. The aqueous solutions of Ga^{3+} and Ni^{3+} were mixed together to yield the desired stoichiometry of the final nanocrystals. A certain amount of SDBS and 60.0 mL deionized water were added to the mixed solutions and stirred vigorously. Subsequently, the pH of the mixed solution was adjusted to 8 by adding $NH_3 \cdot H_2O$. The above solution was transferred into a 100 mL Teflon autoclave, sealed and heated at 170 °C or 150 °C for 10h. After the autoclave was cooled naturally to the room temperature, the resulting precipitates was collected by centrifugation, and washed several times with deionized water and ethanol successively, then dried at 80 ^{o}C overnight. And subsequently the as-prepared samples were calcined in air at 300 °C, 400 °C, 500 °C, 600 °C, 700 °C and 800 °C, respectively for 5 h. Table.1 shows the parameters of the experiment.

2.3 Characterization

The crystalline phase of the products was studied by X-Ray diffraction (XRD) measurement which were performed on D8 advance X-ray diffractometer (Bruker, Switzerland) with Cu Kα radiation (λ = 1.54056 Å) and a scanning speed of 0.2°/min and the Raman spectroscopy (Renishaw in Via) using a 785 nm excitation. Differential Thermal Analysis (DTA) and Thermogravimetricanalysis (TG) were carried out with a NETZSCH STA-449C simultaneous TG-DTA apparatus with a heating rate of 10 K min^{-1} in air to analyze its thermal properties. The morphology and microstructure of the products were characterized by a Scanning Electron Microscope (SEM, Nova NanoSEM430, FEI, Netherlands) equipped with an energy-dispersive X-ray spectrometer (EDS) and a Transmission Electron Microscope (TEM, FEI, Netherlands). Selected Area Electron Diffraction (SAED) patterns were also performed using FEI transmission electron microscope. The diffuse reflectance absorption spectra were recorded using Perkin-Elmer Lambda 900 wide-range spectrophotometer equipped with an integrating sphere. The steady photoluminescence (PL) spectra and lifetime decay curves were recorded on an Edinburgh Instruments FLS920 spectrofluorometer. Magnetic hysteresis loops were obtained by Physical Property Measurement System (PPMS, Quantum Design, USA). All the measurements were performed at room temperature.

3. Results and discussion

3.1 Phase transition analysis

The phase formation and transition behavior of the studied samples were representatively investigated on the precursors GaOOH, obtained via hydrothermal method at 170 °C for 10 h, under the Ga^{3+} concentration is 10 mol/L and the existence of SDBS (sample No. b-3). The normalized XRD patterns of the precursor GaOOH and the corresponding calcined samples are shown in Fig.1.

From Fig.1(a), sharp diffraction peaks at (110), (130), (111) plane of GaOOH can be clearly observed that are in good agreement with standard position from GaOOH (JCPDS54-0910), which indicates that pure orthorhombic phase of GaOOH was obtained successfully. Fig.1(b)-(d) show the XRD results of products calcined at 400 °C, 500 °C and 600 °C, respectively. It can be observed that all diffraction peaks in the patterns can be indexed to a pure hexagonal phase of α-Ga_2O_3 (JCPDS 06-0503), which indicates that α-Ga_2O_3 can be obtained when the precursors GaOOH calcined below 600°C. What is more, when the calcination temperature rises to 700 °C (Fig.1(e)) and 800 °C (Fig.1(f)), the XRD pattern can be readily identified as the monoclinic phase of β-Ga_2O_3 (JCPDS76-0573). Furthermore, no other impurities phases were detected, which implies that the products are all pure β-Ga_2O_3. Upon other experimental conditions, the results are similar to the above and will not be shown here.

To investigate the effect of Ni^{2+} dopant on crystallinity of β-Ga_2O_3, XRD study was carried out on various concentration Ni^{2+}-doped β-Ga_2O_3. Fig.2(a)-(c) show the XRD patterns of β-Ga_2O_3 doping with different Ni^{2+}-doped concentration, obtained via calcining GaOOH precursor (sample No. d-1,2,3) at 800°C. Compared with the results in Fig.1(f), XRD patterns in Fig.2(a)-(c) show that the sharp diffraction peaks are still maintained and corresponding to the standard XRD pattern of β-Ga_2O_3 (JCPDS76-0573) with the addition of Ni^{2+} ions, and without any other diffraction peaks. The above results demonstrate that the Ni^{2+} ions are successfully introduced into the lattice of β-Ga_2O_3. Combining the analysis above, it is believed that the precursor GaOOH doped with 1%, 3%, 5% Ni^{2+} ions had plausibly to transformed into 1%, 3%, 5% Ni^{2+}-doped β-Ga_2O_3 after calcination at 800 °C, which reveals that hydrothermal route with followed heat treatment is suitable to prepare Ni^{2+}-doped β-Ga_2O_3 nanocrystals. It is noteworthy that the diffraction peaks are less sharp with Ni^{2+}-doped concentration increasement in Fig.2, illustrating the crystallinity of

β-Ga_2O_3 became weaken with enhancement of Ni^{2+} incorporation. However, the crystal form of β-Ga_2O_3 has kept the same with Ni^{2+} incorporation, which indicates that Ni^{2+} ions have been successfully entered into the β-Ga_2O_3 nanocrystals host.

In order to further clarify the phase transformation between the GaOOH and Ga_2O_3 crystalline phase, the thermogravimetry-differential thermal analysis (TG-DTA) curves of the as-prepared GaOOH precursor powders in air atmosphere with a heating rate of 10°C/min are shown in Fig.3. The DTA curve shows a broad endothermic peak from 20 °C to 200 °C, meanwhile, the TG curve exhibits a weight loss in the similar temperature range, which is attributed to the dehydration and vaporization of kinds of GaOOH by-products and some residual organics. In addition, it can be clearly seen that a intense exdothermic peak is at ~400 ^{o}C in the DTA curve, which is due to the formation of the α-Ga_2O_3 crystalline phase, and this result is in accordance with the XRD result that α-Ga_2O_3 crystalline begin to form at ~400 ^{o}C (as the XRD pattern shown in Fig. 1(b)). At the meantime, the weight has lost about 9.5% during this process, which is in good agreement with the theoretical weight loss for the conversion from GaOOH to α-Ga_2O_3[46]. Moreover, there is also an intense endothermic peak in the temperature range of about 750°C~840°C due to the formation of β-Ga_2O_3 crystalline phase, and no obvious weight loss in the TG curve during this process, which further prove the results above are corresponding to the phase transition from α-Ga_2O_3 crystalline to β-Ga_2O_3 crystalline. However, the results above show a little deviation with the XRD result that β-Ga_2O_3 crystalline begin to form at 700°C as the XRD patterns shown in Fig. 1(e), which mainly due to the long time calcinations at this temperature made the phase conversion of α-Ga_2O_3 to β-Ga_2O_3 available. From the above results, it is noticeable that the TG-DTA results agree well with XRD results as shown in Fig.1, which further confirm the formation and phase transformation of GaOOH, α-Ga_2O_3 and β-Ga_2O_3 crystalline.

The normalized Raman spectra of 1% Ni^{2+}-doped GaOOH (sample No. d-1) and its corresponding α, β-Ga_2O_3 nanocrystals obtained at different temperature for representatives are shown in Fig.4. From the spectra, the characteristic Raman bands of GaOOH can be observed in the GaOOH:Ni^{2+} sample (red line), which are in good agreement with the previous work by Zhao et.al[47]. And a remarkable change has occurred in the curves when the GaOOH:Ni^{2+} sample calcined at 500 °C and 800 °C, presenting the spectra of Ga_2O_3, which further demonstrate the phase transformation from the precursor GaOOH to Ga_2O_3 crystalline. In addition, all characteristic Raman bands of the GaOOH:Ni^{2+} sample calcined at 800 °C (purple line) can be well indexed to the peaks of β-Ga_2O_3[23,48]. Thereinto, as proposed in the literature[49], the obvious peaks located in the range from 115 cm^{-1} to 200 cm^{-1} can be assigned to libration and translation of tetrahedra-octahedra, the peaks located from 320 cm^{-1} to 475 cm^{-1} belong to deformation of Ga_2O_6 octahedra; and those peaks upon 625 cm^{-1} can be attributed to the stretching and bending of GaO_4 tetrahedra. However, the Raman spectrum of the GaOOH:Ni^{2+} sample calcined at 500 °C (blue line) displays some differences from that of β-Ga_2O_3, especially, the peaks located between 400 cm^{-1} to 800cm^{-1} related to O-Ga-O stretching or bending modes, which exhibit a relative weaker intensity and a slight blue shift in wavenumber compared with that of β-Ga_2O_3. The difference above is consistent with the variation of Raman spectra during the transition from GaOOH to β-Ga_2O_3 proposed by Zhao et al[47], therefore, it could be suggested that the Raman spectrum of the GaOOH:Ni^{2+} sample calcined at 500 °C is related to α-Ga_2O_3. From the above results, it is noteworthy that the Raman results are well in agreement with XRD and TG-DTA results as mentioned before, which make a further confirmation to the fact that the formation and phase transformation of GaOOH, α-Ga_2O_3 and β-Ga_2O_3 crystalline via hydrothermal route and the subsequent heat treatment.

3.2 Morphology and crystal growth mechanism

The SEM images of as-prepared GaOOH precursors with different experimental conditions are displayed in Fig.5. It can be seen in Fig.5(a) that the SDBS-free GaOOH samples are consisted of relatively uniform and well-dispersed prism-like nanocrystals with a rough surface. The size and length-diameter ratio of these nanoparticles increase as increasing concentrations of Ga^{3+} ions. With the addition of a certain amount of SDBS, Fig.5(b) show that the GaOOH samples with better dispersity present a rice-like morphology gathered with the nanorods ~50 nm in width and 0.7~1 μm in length. Compared the SEM images in Fig.5(a) and Fig.5(b) correspondingly, one can see that GaOOH samples prepared with or without SDBS in the same Ga^{3+} ion concentration present diverse morphology with different length-diameter ratio, which indicates that SDBS as a surfactant has great influence on the crystal growth of the GaOOH nanoparticles and the corresponding growth mechanism will be discussed in detail later. Fig.5(c) illustrate the precursors GaOOH nanoparticles prepared at 150 °C for 10 h with a certain amount of SDBS, which present a slight difference in morphology compared with that obtained at 170 °C for 10 h. On the basis of the results above, the optimized experimental conditions designed to further conduct our studies as follows: the concentration of Ga^{3+} ion is 10 mol/L, hydrothermal condition is 170 °C for 10 h, and with the addition of SDBS(0.1743 g). Moreover, the SEM images of the Ni^{2+}-doped GaOOH samples prepared under the above conditions were also displayed in Fig.6. With an enhancement of Ni^{2+}-doped concentration, the morphologies and size of GaOOH samples have varied slightly, retaining the rice-like structure assembled with orderly oriented and monodisperse nanorods, but it is remarkable that these nanorods are much slenderer and longer, with a higher aspect-ratio as the doping concentration of Ni^{2+} ions(1%, 3% to 5%) increase. The SEM images of as-prepared Ni^{2+}-doped GaOOH samples calcined at 500 °C and 800 °C are shown in Fig.6(d') and Fig.6(d''),

respectively. It is noteworthy that the morphology of the calcined samples still maintains the rice-like structure, but the size becomes smaller as elevating the calcination temperature, which may due to the dehydration and decomposition process as proposed in the TG-DTA result. From the above results, it can be concluded that monodisperse rice-like Ga_2O_3 nanocrystals can be successfully synthesized via hydrothermal method with a subsequent calcination combined with the XRD, TG-DTA and Raman results above. What is more, it can be deduced that the critical factors to control the crystal growth and morphology of Ga_2O_3 nanocrystals are both the surfactant SDBS and the Ni^{2+}-doped concentration in the hydrothermal treatment, but not the subsequent calcination process.

The morphology, size and crystal structure of 5% Ni^{2+}-doped β-Ga_2O_3 nanocrystals (d-3 calcined at 800 °C) were further characterized by TEM and HRTEM. A typical TEM image of the 5% Ni^{2+}-doped β-Ga_2O_3 in Fig.7(a) shows that the uniform nanorods with a smooth surface exhibit an average diameter of ~50 nm along their entire length, which agrees well with the SEM results above. Fig.7(b) presents the HRTEM image of Ni^{2+}-doped β-Ga_2O_3 nanorods, revealing that the clear crystal lattice fringes with the spacing d value of ~0.255 nm corresponds to a (111) crystal facet of the β-Ga_2O_3 phase. In addition, the insert of Fig.7(b) shows the corresponding selected area electron diffraction (SAED) pattern of an individual rice-like β-Ga_2O_3 nanorod, reveals the polycrystalline character of the nanorod, which further confirms that the rice-like nanorod is composed of bundles of sharp nanofibers. Moreover, the SAED pattern can be well indexed to the pure monoclinic phase of β-Ga_2O_3. To investigate the introduction and distribution of Ni^{2+} ions in the lattice of β-Ga_2O_3 nanocrystals, the EDS spectra of β-Ga_2O_3 nanocrystals was shown in Fig.7(f), where the peaks according to the designed elements (Ga, O and Ni) are clearly observed. What's more, The EDS elemental mapping distribution of Ga, O and Ni image were illustrated in Figs. 7(c,

d, e). The distribution region of Ga, O and Ni elements are almost overlapping, which confirms that the Ni^{2+} ions have entered into the lattice of Ga_2O_3 nanocrystals. And line scan was also carried out in the direction perpendicular to the axial direction of the nanocrystal to further investigate the distribution of Ga, O and Ni elements in the nanocrystals. The forms of Ga, O and Ni profiles in line scan indicated that Ni dopants was distributed homogeneously (Fig.7 (g)).

As mentioned above, both the surfactant SDBS and the Ni^{2+}-doped concentration have great effects on the crystal growth and morphology of Ga_2O_3 nanocrystals in the hydrothermal treatment. Thereinto, a schematic illustration of the crystal growth of GaOOH nano-structure is shown in Fig. 8 and the possible formation mechanism is proposed as follows. Generally, the formation process of GaOOH nanocrystals includes nucleus-formation, gathering, oriented growth, and self-assembling. During the hydrothermal treatment process, the surfactant-free GaOOH nucleus gather quickly growing into a small prism-shape nanorods, and self-assembling to the prism-shaped nanostructures (Fig. 5(a)) may due to the electrostatic effect built up in the surface of nanorods, which leading to a strengthening of attraction among the nanorods. However, when the addition of SDBS as a surfactant, the SDBS is hydrolyzed into DBS^- anion which coordinates with Ga^{3+} ions soon to form a Ga^{3+}–$3DBS^-$ complex due to the single electron on sulphur atoms as stage-I displayed in Fig. 8. As a result, the concentration of free Ga^{3+} ions in the solution system can be effectively reduced, meanwhile, give rise to a diminishment of the nucleation and crystal growth rate, which leading to the effective separation of nucleation and growth process and thus facilitating the formation of GaOOH nanorods with relatively high quality[50-52]. In addition, the free DBS^- can also selectively cap on the side of GaOOH nucleus, resulting in a GaOOH nanorods with higher length-diameter ratio due to the anisotropic growth. GaOOH nanorods with different length self-assembled into a rice-shaped GaOOH nanostructure as presented. in Fig.5(b) and (c) (stage-II in Fig.8).What is more,

higher aspect ratio was also found in the GaOOH nanocrystals with the Ni^{2+}-doped concentration increases, which may also be related to the chelation between the metal ions (Ga^{3+} and Ni^{2+}) and surfactant SDBS. As mentioned above, Ga^{3+}/Ni^{2+} ions could form a Ga^{3+}–$3DBS^{-}/Ni^{2+}$–$2DBS^{-}$ complex with the hydrolyzed DBS^{-} ions, while the Ni^{2+}–$2DBS^{-}$ displays a more flexible and rapid movement in the nucleation process for its less DBS^{-}, which leads to an enhancement of crystal growth process facilitating the GaOOH nanorods with stronger anisotropic growth into the nanofibers with a higher aspect ratio. GaOOH nanofibers self-assemble into a rice-shaped GaOOH nanostructure as presented in Fig.6(d) (stage-II in Fig.8). It is noteworthy that the self-assembled morphology was also suggested in the Ga-based compounds and the surfactant assisted systems[25,53-54]. Its formation and stabilization might be related with its surface energy or stress[18-19]. Ultimately, with the surfactant SDBS and the various Ni^{2+}-doped concentration, the GaOOH nanorods can be obtained with diverse aspect ratio, self-assembling into a rice-like nanostructure. However, the growth mechanism of rice-like GaOOH nanostructure proposed above is built upon the experimental results and previous reports, and the detailed process have not clarified yet.

3.3 Optical properties

Generally, doping will destroy the crystallinity of nanocrystals and thus causing charge imbalance around doping lattice. Consequently, electronic field can be introduced via interaction of doping ions and nanocrystal lattice, which result in splitting of energy level and thus removing degeneracy of doping ions that can alter the electronic transition of it. Therefore, to investigate the electronic transition of different Ni^{2+}-doped β-Ga_2O_3 nanostructures, optical diffuse reflectance absorption spectra of β-Ga_2O_3 nanostructures with different Ni^{2+}-doped concentrations (0%, 1%, 3%, 5%) are presented in Fig.9. When introduction of Ni^{2+} ions into β-Ga_2O_3 nanostructures, it is clearly found in Fig.9 that the absorption spectra consist of three main absorption bands centered at

around 395 nm, 640 nm, 1085 nm, which are assigned to the spin-allowed $^3A_{2g}$ (^3F)→$^3T_{1g}$ (^3P), $^3T_{1g}$ (^3F) and $^3T_{2g}$ (^3F) transitions of Ni^{2+} in octahedral sites, respectively[29,32,35,55]. Moreover, these characteristic absorption peaks in Fig. 9 display an obvious red shift with enhancement of Ni^{2+} dopants, which maybe due to the Ni^{2+} dopants decrease the crystallinity as suggested in the XRD results in Fig. 2, leading to weaken crystal field of β-Ga_2O_3. Actually, with an in depth insight in it, these absorption peaks can be ascribed to the *d*-orbitals energy level splitting of Ni^{2+} ion in octahedral symmetry. And based on the crystal field theory, the fivefold degenerate 3d-states of Ni^{2+} are split into doubly degenerate *e*-states (higher in energy), which span the Fermi energy, and threefold degenerate t_2-states near the top of the valence bands. Furthermore, two weak absorption peaks centering at around 485 nm and 775 nm of the three doped samples are attributed to the spin-forbidden $^3A_{2g}$ (^3F)→$^1T_{2g}$ (^1D) and $^3A_{2g}$ (^3F)→$^1E_{1g}$ (^1D) transitions, respectively[33].

As known to all, the optical properties of transition metal ions doped nanocrystal materials were is hypersensitive to the crystal field environment surround the transition metal ions. Herein, the PL excitation and emission spectra of β-Ga_2O_3 nanostructures with different Ni^{2+}-doped concentrations (0%, 1%, 3%, 5%) are shown in Fig.10 and Fig.11, respectively. It can be clearly seen in Fig.10 that the excitation spectra monitored at 1450 nm are mainly comprised of four broad bands: two intense broad bands with peak centers at around 262 nm and 318 nm correspond to the intrinsic excitation of β-Ga_2O_3 host lattice caused by charge migration, and two relatively weak bands centered at around 400 nm and 690 nm are attributed to the typical transition from the ground state $^3A_{2g}$ (^3F) to the excited stated $^3T_{1g}$ (^3P), $^3T_{1g}$ (^3F) of Ni^{2+} ions, which agrees well with the results of absorption spectra in Fig.9. Upon the excitation of 262nm, 318nm and 400 nm, a broadband emission from 1200 nm to 1600 nm with a maximum around 1450 nm can be observed in β-Ga_2O_3:Ni^{2+} nanocrystals in Fig.11(a) (PL spectra under 262 nm and 400 nm excitation are

similar to that in Fig.11(a), and thus were not shown here), and one should be known that the near-infrared emission under excitation of intrinsic excitation of β-Ga_2O_3 host lattice can be contributed to the energy transfer from the host lattice to Ni^{2+}. However, the broadband near-infrared emission can't be observed in α-Ga_2O_3 at the same condition (not listed). The interesting phenomenon mentioned above may due to β-Ga_2O_3 crystal lattice can provide the octahedral doping sites for Ni^{2+} ions to form the octahedral coordinated Ni^{2+} ions giving rise to a near-infrared emission, however, no octahedral sites exist in α-Ga_2O_3 crystal lattice. In addition, the PL spectra results further illustrate that the Ni^{2+} ions have been successfully doped into the lattice of β-Ga_2O_3 nanocrystals. What is more, it is remarkable that the broad emission band centered at 1450 nm can be assigned to the characteristic $^3T_{2g}$ (^3F)→$^3A_{2g}$ (^3F) transition corresponding to the octahedral Ni^{2+} ions. As depicted in Fig.11(a) and (b), the intensity of the near-infrared emission decreases while the peak presents a slight red shift with the raise of Ni^{2+}-doping concentration in β-Ga_2O_3 nanocrystals, which are consistent with the results of absorption spectra in Fig.9. Moreover, Fig.12 illustrates the corresponding decay curve of the 1% and 3% Ni^{2+}-doped β-Ga_2O_3 nanostructures. By the single-exponential function, the fluorescence lifetime of 1%, 3% Ni^{2+}-doped β-Ga_2O_3 was fitted to about 367 μs and 296 μs, respectively. Based on the results above, the near-infrared emission intensity and corresponding lifetime diminish with the increase of Ni^{2+}-doped concentration, which may be also due to the crystal field of β-Ga_2O_3 becomes weaker as suggested in the result of absorption spectra. Moreover, as the previous work[27] suggested, the weaken of near-infrared emission may be also due to the possibility of multiphonon relaxation would increase along with the enhancement of Ni^{2+}-doped concentration. It is noteworthy that the intense suppression of near-infrared emission corresponding to 5% Ni^{2+}-doped β-Ga_2O_3 nanocrystals may be due to the concentration quenching related with lower activation energy of

nonradiative relaxation process. As noted before, crystal environment around Ni^{2+} ions has a great effect on optical properties of Ni^{2+} ions for their electrons in outer *d* orbit will have a strong interactation with β-Ga_2O_3 host lattice, and thus the crystal field strength is recognized as a direct factor to influence optical properties in the Ni^{2+}-doped β-Ga_2O_3 nanocrystals[56]. On the basis of the XRD, absorption spectra and PL spectra results above, it can be deduced that both the crystallinity and crystal field of β-Ga_2O_3 would decrease as the increase of Ni^{2+} dopants concentration.

Therefore, according to Tanabe–Sugano diagram[57], slight red shift of the emission can be detected here. To demonstrate this assumption, it is essential to make further investigation on the variation of crystal field strength of Ni^{2+}- doped β-Ga_2O_3. Thus, the diffuse reflectance absorption spectra was recalled to calculate crystal field strength of Ni^{2+}-doped β-Ga_2O_3.The crystal field parameter Dq can be estimated by wavenumbers of v_1 band based on the expression: $Dq=v_1/10$[29], accordingly, crystal field strength of β-Ga_2O_3 with 1%, 3% and 5% Ni^{2+}-doped concentration was calculated about 938 cm^{-1}, 917 cm^{-1} and 897 cm^{-1}, respectively. And the relative TS diagram of these Ni^{2+}-doped β-Ga_2O_3 was proposed in Fig.13. These data were consistent with XRD results and indicated crystal field strength of β-Ga_2O_3 is truly weaker with higher Ni^{2+}-doped concentration as depicted in Fig.13, resulting in the red shift of near-infrared emission of Ni^{2+} ions, which are in well accordance with the absorption spectra and PL spectra results above. As described before, the crystallinity of β-Ga_2O_3 decreased by Ni^{2+} non-equivalently occupying at the Ga^{3+} sites, leading to a diminishment of crystal field of β-Ga_2O_3. And more Ni^{2+} ions introduced into–the β-Ga_2O_3 crystal structure contribute to much more distortion of the crystal and more weak crystal field of β-Ga_2O_3, consequently, resulting in a reduction of Dq value. It is worthwhile to note that the broadband emission of Ni^{2+}-doped β-Ga_2O_3 with full width at half maximum reach about 300nm has successfully cover the wavebands of both double optical communication window (1310 nm, 1550

nm) and the second biological transparent window (1000 nm ~ 1350 nm), promising attractive potential applications in the optical and biomedical fields.

3.4 Magnetic property and possible optical-magnetic (OM) function of Ni^{2+}-doped β-Ga_2O_3

With the hope of obtaining optical-magnetic (OM) bifunctional materials in single phase Ni^{2+}-doped β-Ga_2O_3, magnetic investigations of Ni^{2+}-doped β-Ga_2O_3 are also carried out in this work, to our best knowledge, which have not been reported before. It is proposed by previous report [58] that replacement the octahedral sites of β-Ga_2O_3 with Ni^{2+} ions may introduce ferromagnetic state into the β-Ga_2O_3 nanocrystal. To further validate the magnetic property in the Ni^{2+}-doped β-Ga_2O_3 nanocrystals, the magnetization versus magnetic field (M–H) curves of β-Ga_2O_3 nanocrystals with different Ni^{2+}-doped concentration carried out by PPMS are presented in Fig.14. It can be observed that the hysteresis loop of undoped nanocrystals (in Fig.14, black line) exhibits a paramagnetic nature at room temperature. In addition, the enlarged diagram describes a slight coercive force about 15 Oe in the insert of Fig.14, which may be ascribed to the impurities in the undoped β-Ga_2O_3 nanocrystals. However, the β-Ga_2O_3 nanocrystals with 1%, 3%, 5% Ni^{2+}-doped concentrations reveal a relatively high magnetic coercive force and remnant magnetization in Fig.14, which indicates that ferromagnetic (FM) nature only exists in the Ni^{2+}-doped β-Ga_2O_3 nanocrystals at room temperature. It can be deduced from the above result that the introduction of Ni^{2+} ions have great influence on the magnetism of β-Ga_2O_3 nanocrystals and endow the β-Ga_2O_3 nanocrystals with a significant ferromagnetic property. In addition, the magnetic parameters of M–H curves corresponding to Ni^{2+}-doped β-Ga_2O_3 in Fig.14 are detailedly listed in Table.2. Notably, the value of Hc corresponding to Ni^{2+}-doped β-Ga_2O_3 shows a tendency of enlargement with the Ni^{2+}-doped concentration increase, which provides a further verification that the Ni^{2+} ions induce the FM state in β-Ga_2O_3 as noted before. On the basis of the first-principles spin-polarized density functional

theory, meanwhile according to the previous references[58-59], the ferromagnetism of Ni^{2+}-doped β-Ga_2O_3 nanocrystals may be mainly ascribed to two factors as follows: the most important is the exchange interactions between transition metal (TM) ions and O^{2-} ions spin moments, as demonstrated by theoretical calculations[58], which is induced by Ni-3d and O-2p spin moments and similar to those TM ions doped ZnO systems[59-61]. Another one is the distortion of crystal lattice and the increase of defect states caused by Ni^{2+} dopants in the β-Ga_2O_3 nanocrystals as suggested above, which will responsible for the formation of a spin-polarized impurity band. Furthermore, the impurity band has the possibility of overlapping with empty d band and thus causing charge transfer [62-65]. Besides, a significant diminishment of Ms and Mr values is observed in Fig.14 when the doping concentration is increased, which indicates the hard magnetic property of Ni^{2+}-doped β-Ga_2O_3 nanocrystals tends to enhance gradually with the Ni^{2+} dopants concentration increase. What's more, it can also be found that the hysteresis loops show a slight migration, exhibiting the exchange anisotropy, which may be attributed to ferromagnetic (FM) and antiferromagnetic (AFM) exchange mechanism[66]. It should also be noted that the β-Ga_2O_3 nanocrystals with high Ni^{2+} doping concentration present a little diamagnetism property, similar to the curve of the undoped β-Ga_2O_3 nanocrystals, which may be due to the changing of orbit moment introduced by Larmor precession.

Herein, it can be concluded that magnetic properties were successfully realized in the Ni^{2+}-doped β-Ga_2O_3 nanocrystals, accordingly, the single phase materials endow both the optical and magnetic properties were successfully obtained in the Ni^{2+}-doped β-Ga_2O_3 nanocrystals. Which is remarkably meaningful for magneto-optical interaction mainly occur at atoms scale[67]. The Ni^{2+}-doped β-Ga_2O_3 nanocrystals as magneto-optical materials have promising potential application in the fields of optical communication, biological diagnosis and magnetic information storage, et al.

Further investigation on manipulating its optical properties via plus magnetic fields seems relatable scientific interest.

4. Conclusions

In summary, the monodisperse rice-like Ni^{2+}-doped α, β-Ga_2O_3 nanostructures are successfully synthesized by a mild hydrothermal route and calcination process. The phase transition occurs from the precursor GaOOH, α-Ga_2O_3 to β-Ga_2O_3 crystalline phase when calcining precursors at different temperature. Both the surfactant SDBS and Ni^{2+} doping concentration have great effect on the morphology of the β-Ga_2O_3 nanostructures, and a growth mechanism corresponding to the rice-like Ni^{2+}-doped GaOOH nanostructures is also proposed. The Ni^{2+}-doped β-Ga_2O_3 nanocrystals give rise to a broadband NIR luminescence from 1200 nm to 1600 nm with a maximum around 1450 nm, covering the optical communication and the second biological transparent window, which hold great promise for the optical and biomedical fields. In addition, the single phase Ni^{2+}-doped β-Ga_2O_3 nanocrystals exhibit a ferromagnetic nature. Ultimately, the bifunctional materials equipped with both NIR luminescence and magnetic properties in a single phase are realized in the Ni^{2+}-doped β-Ga_2O_3 nanocrystal, which would turn into an excellent candidate for potential application in the fields of optical communication, biological diagnosis and magnetic information storage, etc.

Acknowledgements

This work was supported by the National Natural Science Foundation of China (61475047, 51102096), the Fundamental Research Funds for the Central Universities (2013ZM0001), and the project of Guangzhou Pearl River Science and Technology New Star. The authors are grateful to

Miss X.S. Zhang for a part of sample preparation, and Dr. G. Wang for his fruitful discussion about magnetic property.

References:

[1] M. Corricelli, N. Depalo, E. Di Carlo, E. Fanizza, V. Laquintana, N. Denora, A. Agostiano, M. Striccoli and M. L. Curri, Nanoscale, 2014, 6,7924–7933.
[2] Z. Jiang, N. Dai, L. Yang, J. Peng, H. Li, J. Li and W. Liu, J. Non-Cryst. Solids, 2014, 383, 196–199.
[3] J. Wu and J. L. Coffer, J. Phys. Chem. C, 2007, 111,16088–16091.
[4] T. Lin, X. Zhang, J. Xu, X. Liu, M. T. Swihart, L. Xu and K. Chen, Appl. Phys. Lett., 2013, 103, 181906.
[5] G. Dong, M. Liang, H. Qin, G. Chai, X. Zhang, Z. Ma, M. Peng and J. Qiu, Phys. Chem. Chem. Phys., 2012, 14, 13594–13600.
[6] Y. Zhao, R. L. Frost, J. Yang and W. N. Martens, J. Phys. Chem. C, 2008, 112, 3568–3579.
[7] T. Weh, J. Frank, M. Fleischer and H. Meixner, Sens.Actuators, B, 2001, 78, 202–207.
[8] K. Shimizu, A. Satsuma and T. Hattori, Appl. Catal., 1998, 16, 319-326.
[9] P. P. Pescarmona, K. P. F. Janssen and P. a Jacobs, Chem. Eur. J., 2007, 13, 6562–6572.
[10] P. Pescarmona and P. Jacobs, Catal. Today, 2008, 137, 52–60.
[11] M. Ogita, N. Saika, Y. Nakanishi, Y. Hatanaka, Appl. Surf. Sci., 1999, 142, 188–191.
[12] K. Nakagawa, C. Kajita, Y. Ide, M. Okamura, S. Kato and H. Kasuya, Catal. Lett., 2000, 64, 215–221.
[13] W. Jochum, S. Penner, R. Kramer, K. Fottinger, G. Rupprechter and B. Klotzer, J. Catal., 2008, 256, 278–286.
[14] W. Jochum, S. Penner, K. Fottinger, R. Kramer, G. Rupprechter and B. Klotzer, J. Catal., 2008, 256, 268–277.
[15] C. A. Deshmane, J. B. Jasinski and M. A. Carreon, Microporous Mesoporous Mater., 2010, 130, 97–102.
[16] A.C. Tas, P. J. Majewski and F. Aldinger, J. Am. Ceram. Soc., 2002, 85, 1421–1429.
[17] T. Wang, S. S. Farvid, M. Abulikemu, and P. V. Radovanovic, J. Am. Chem. Soc., 2010, 132, 9250-9252.
[18] S. S. Farvid, N. Dave, and P. V. Radovanovic, Chem. Mater., 2010, 22, 9.
[19] S. S. Farvid, N. Dave, T. Wang, and P. V. Radovanovic, J. Phys. Chem. C, 2009, 113, 15928.
[20] M. Zinkevich and F. Aldinger, J. Am. Ceram. Soc., 2004, 87,683-691.
[21] A. W. Laubengayer and H. R. Engle, J. Am. Chem. Soc., 1939, 61, 1210–1214.
[22] M. R. Delgado, C. O. Areάn, Z. Anorg. Allg. Chem., 2005, 631, 2115–2120.
[23] X. Wang, Q. Xu, M. Li, S. Shen, X. Wang, Y. Wang and Z. Feng, Angew. Chem. Int. Ed., 2012, 51, 13089–13092.
[24] K. Irmscher, Z. Galazka, M. Pietsch, R. Uecker and R. Fornari, J. Appl.Phys., 2014,110, 063720.
[25] G. Li, C. Peng, C. Li, P. Yang, Z. Hou, Y. Fan, Z. Cheng and J. Lin, Inorg. Chem., 2010, 49, 1449–1457.
[26] G. K. B. Costa, L. P. Sosman, A. López, N. Cella and R. B. Barthem, J. Alloys Compd., 2012, 534, 110–114.
[27] S. Zhou, G. Feng, B. Wu, N. Jiang, S. Xu and J. Qiu, J. Phys. Chem. C, 2007, 111, 7335–7338.
[28] V. N. Sigaev, N. V Golubev, E. S. Ignat, V. I. Savinkov, M. Campione, R. Lorenzi, F. Meinardi and A. Paleari, Nanotechnology, 2012, 23, 015708.
[29] H. Shigemura, M. Shojiya, R. Kanno and Y. Kawamoto, J. Phys. Chem. B, 1998, 102, 1920–1925.
[30] T. Suzuki and Y. Ohishi, Appl. Phys. Lett., 2004, 84, 3804.
[31] T. Suzuki, S. Murugan and Y. Ohishi, Appl. Phys. Lett., 2005, 86, 131903.
[32] M. L. Pang, W. Y. Shen and J. Lin, J. Appl. Phys., 2005, 97, 033511.
[33] B. Wu, S. Zhou, J. Ren, D. Chen, X. Jiang, C. Zhu and J. Qiu, Appl. Phys. B, 2007, 87, 697–699.
[34] S. Zhou, H. Dong, G. Feng, B. Wu, H. Zeng and J. Qiu, Opt. Express, 2007, 15, 5477–5481.

[35] B. Wu, J. Qiu, N. Jiang, S. Zhou, J. Ren, D. Chen, X. Jiang and C. Zhu, J. Mater. Res., 2007, 22, 3410–3414.
[36] J. Bridot, A. Faure, S. Laurent, C. Rivie, C. Billotey, B. Hiba, M. Janier, J. Coll, L. Vander Elst, R. Muller, P. Perriat, O. Tillement, C. B. Lyon, V. Cedex, G. De Recherche, U. Inserm, I. A. Bonniot and L. T. Cedex, J. Am. Chem. Soc., 2007, 129, 5076–5084.
[37] H. Gu, R. Zheng, X. Zhang and B. Xu, J. Am. Chem. Soc., 2004, 126, 5664–5665.
[38] H. Kim, M. Achermann, L. P. Balet, J. a Hollingsworth and V. I. Klimov, J. Am. Chem. Soc., 2005, 127, 544–546.
[39] G. Wang, Q. Peng and Y. Li, Acc. Chem. Res., 2011, 44, 322–332.
[40] Y. X. Ma, H. Li and L. Wang, J. Mater. Chem., 2012, 22, 18761–18767.
[41] J. Beltran-Huarac, M. J. Guinel, B. R. Weiner and G. Morell, Mater. Lett., 2013, 98, 108–111.
[42] H. Peng, B. Cui, L. Li and Y. Wang, J. Alloys Compd., 2012, 531, 30–33.

[43] V. K. Tikhomirov, L. F. Chibotaru, D. Saurel, P. Gredin, M. Mortier and V. V Moshchalkov, Nano Lett.,2009, 9, 721-724.
[44] S.K. Singh, K. Kumar, M.K. Srivastava, D.K. Rai and S.B. Rai, Opt.Lett., 2010, 35, 1575–1577.
[45] Y. Liu, H. Liu, Z. Chen, N. Kadasala, C. Mao, Y. Wang, Y. Zhang, H. Liu, Y. Liu, J. Yang and Y. Yan, J. Alloys Compd., 2014, 604, 281–285.
[46] X. Liu, G. Qiu, Y. Zhao, N. Zhang and R. Yi, J. Alloys Compd., 2007, 439, 275–278.
[47] Y. Zhao, J. Yang and R. L. Frost, J. Raman Spectrosc., 2008,39, 1327–1331.
[48] H. J. Chun and Y. S. Choi, J. Phys. Chem. B, 2003, 107, 9042–9046.
[49] R. Rao, A. M. Rao, B. Xu, J. Dong, S. Sharma and M. K. Sunkara, J. Appl. Phys., 2005, 98, 094312.
[50] F. He, N. Niu, L. Wang, J. Xu, Y. Wang, G. Yang, S. Gai and P. Yang, Dalton Trans., 2013, 42, 10019–10028.
[51] Q. Sun, X.Q. Zhang, F. Han, W.C. Li and A.H. Lu, J. Mater. Chem., 2012, 22, 17049.
[52] Y. Xie, Q.R. Zhao, T. Dong, Z.G. Zhang, J. Phys. Chem. C, 2007, 111, 11598-11603.
[53] L. Li, W. Wei and M. Behrens, Solid State Sci., 2012, 14, 971–981.
[54] Y. Zhao, R. L. Frost, J. Yang and W. N. Martens, J. Phys. Chem. C, 2008, 112, 3568–3579.
[55] S. Zhou, N. Jiang, H. Dong, H. Zeng, J. Hao and J. Qiu, Nanotechnology, 2008, 19, 015702.
[56] H.T. Sun, F. Shimaoka and J. Ruan et al., J. Non-Cryst. Solids, 2009,355, 2425-2428.
[57] Y. Tanabe, S.Sugano, J. Phys. Soc. Jpn., 1954, 9, 753-766.
[58] W. Xiao, L. Wang, L. Xu and B. S. Zou, Scr. Mater., 2009, 61, 477–480.
[59] B. Babu, G. R. Sundari, K. Ravindranadh, M. R. Yadav and R. V. S. S. N. Ravikumar, J. Magn. Magn. Mater., 2014, 372, 79–85.
[60] Y. Liu, J. Yang, Q. Guan, L. Yang, Y. Zhang, Y. Wang, B. Feng, J. Cao, X. Liu, Y. Yang and M. Wei, J. Alloys Compd., 2009, 486, 835–838.
[61] E. Liu, P. Xiao, J. S. Chen, B. C. Lim and L. Li, Curr. Appl. Phys., 2008, 8, 408–411.
[62] J. M. D. Coey, M. Venkatesan and C. B. Fitzgerald, Nat. Mater., 2005, 4, 173.
[63] P.V. Radovanovic and D. R. Gamelin, Phys. Rev. Lett., 2003, 91, 157202.
[64] J. M. D. Coey, K.Wongsaprom, J. Alaria and M. Venkatesan, J. Phys. D, 2008, 41, 134012.
[65] S.S. Farvid,. T. Sabergharesou, L.N. Hutfluss, M. Hegde, E. Prouzet, and P.V. Radovanovic, J. Am. Chem. Soc., 2014, 136, 7669−7679.
[66] D. Chu, Y. P. Zeng and D. Jiang, Solid State Commun., 2007, 143, 308–312.
[67] Y. Liu, D. Wang, J. Shi, Q. Peng and Y. Li, Angew. Chem. Int. Ed. Engl., 2013, 52, 4366–4369.

Table/Figures and captions

Table.1 Experimental parameters.

Table.2 The magnetic parameters of M–H curves corresponding to Ni^{2+}-doped β-Ga_2O_3 in **Fig.14**.

Fig.1 XRD patterns of (a) GaOOH precursor (10 mol/L of Ga^{3+}) obtained at 170 °C/10 h, with SBDS (sample No.b-3); and the samples calcined at (b) 400 °C; (c) 500 °C; (d) 600°C as α-Ga_2O_3 and (e) 700°C; (f) 800 °C as β-Ga_2O_3.

Fig.2 XRD patterns of β-Ga_2O_3 with different Ni^{2+}-doped concentration of 1%, 3% and 5%, calcined at 800 °C from GaOOH precursor (10 mol/L of Ga^{3+}) obtained at 170 °C/10 h with SBDS (sample No.b-3).

Fig.3 TG-DTA curves of GaOOH obtained at 170 °C/10 h, in 10 mol/L ionic concentration, with SBDS (sample No.b-3).

Fig.4 Raman spectra of 1% Ni^{2+}-doped GaOOH, α-Ga_2O_3 and β-Ga_2O_3 (sample No. d-1).

Fig.5 Typical SEM images of GaOOH under different experimental conditions: (x-1), (x-1), (x-3){x=a,b,c} are in 0.8, 5, 10 mol/L of Ga^{3+}, respectively. (a-1)~(a-3) are under 170 °C/10 h, without SDBS; (b-1)~(b-3) are under 170 °C/10 h, with SDBS; and (c-1)~(c-3) are under 150 °C/10 h, with SDBS. All the scale bar is 500nm.

Fig.6 Typical SEM images of (d-1)~(d-3): GaOOH with 1%, 3%, 5% Ni^{2+}-doped, respectively (170 °C/10h, with SDBS, 10 mol/L of Ga^{3+}); (d-1)'~(d-3)': 600°C calcination products as α-Ga_2O_3 from (d-1)~(d-3), respectively; and (d-1)''~(d-3)'':800 °C calcination products as β-Ga_2O_3 from (d-1)~(d-3), respectively. All the scale bar is 500nm.

Fig.7 (a) TEM, (b) HR-TEM and SAED images (inset), (c, d, e) Ga, O and Ni EDS elemental maps, (f) EDS spectra and (g) EDS line scan profile of 5% Ni^{2+}-doped β-Ga_2O_3 obtained at 800 °C (170 °C/10 h, with SDBS, 10 mol/L of Ga^{3+}).

Fig.8 Growth mechanism of the GaOOH nanocrystals.

Fig.9 Diffuse reflectance absorption spectra of 0%, 1%, 3%, 5% Ni^{2+}-doped β-Ga_2O_3 obtained at 800 °C (170 °C/10 h, with SDBS, 10 mol/L of Ga^{3+}).

Fig.10 PL excitation spectra of different concentration of Ni^{2+} doped β-Ga_2O_3.

Fig.11 (a) PL emission spectra of different concentration of Ni^{2+}-doped β-Ga_2O_3 under 318nm excitation, and (b) normalized PL emission spectra of 1%, 3% Ni^{2+}-doped β-Ga_2O_3 (inset is the amplified PL spectra).

Fig.12 PL decay curve of 1%, 3% Ni^{2+}-doped β-Ga_2O_3.

Fig.13 Tanabe–Sugano (TS) diagram of Ni^{2+}-doped β-Ga_2O_3.

Fig14 M–H curves of 0%, 1%, 3%, 5% Ni^{2+}-doped β-Ga_2O_3 (inset is the amplified M–H curves of 0%, 1%, 3%, 5% Ni^{2+}-doped β-Ga_2O_3).

Table.1 Experimental parameters.

Sample No.	Ionic concentration (M)	Ga^{3+} (0.5 M)	Ni^{2+} (0.05 M)	SBDS (g)	Hydrothermal condition
a-1	0.8	100%	0	0	170 °C, 10 h
a-2	5	100%	0	0	170 °C, 10 h
a-3	10	100%	0	0	170 °C, 10 h
b-1	0.8	100%	0	0.0279	170 °C, 10 h
b-2	5	100%	0	0.1743	170 °C, 10 h
b-3	10	100%	0	0.3485	170 °C, 10 h
c-1	0.8	100%	0	0.0279	150 °C, 10 h
c-2	5	100%	0	0.1743	150 °C, 10 h
c-3	10	100%	0	0.3485	150 °C, 10 h
d-1	5	99%	1%	0.1743	170 °C, 10 h
d-2	5	97%	3%	0.1743	170 °C, 10 h
d-3	5	95%	5%	0.1743	170 °C, 10 h

Table.2 The magnetic parameters of M–H curves corresponding to Ni^{2+}-doped β-Ga_2O_3 in **Fig.14**.

sample	saturation magnetization (Ms) (emu/g)	coercive force (Hc) (Oe)	remnant Magnetization (Mr) (emu/g)	magnetic property
β-Ga_2O_3	—	~15	—	paramagnetic
1%Ni^{2+}:β-Ga_2O_3	2.15×10^{-2}	80~100	3.0×10^{-3}	ferromagnetic
3%Ni^{2+}:β-Ga_2O_3	2.6×10^{-3}	120~170	8×10^{-4}	ferromagnetic
5%Ni^{2+}:β-Ga_2O_3	1.5×10^{-3}	100~250	2.7×10^{-4}	ferromagnetic

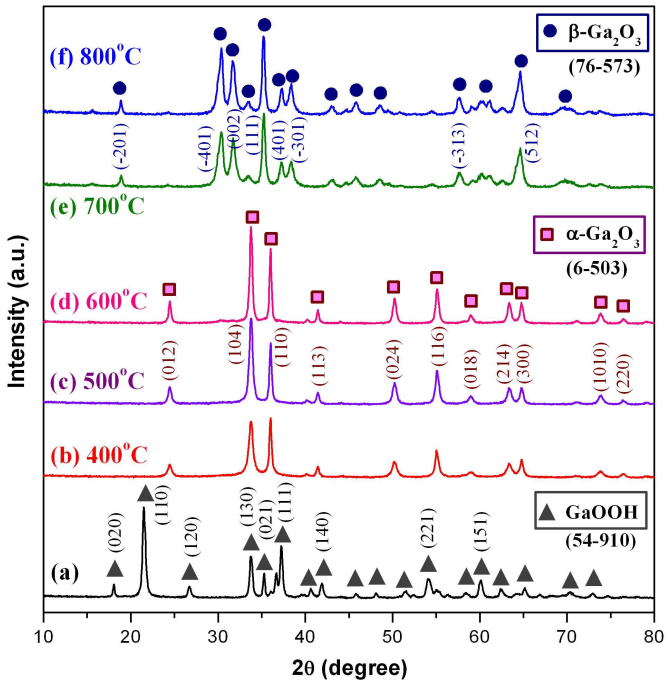

Fig.1 XRD patterns of (a) GaOOH precursor (10 mol/L of Ga^{3+}) obtained at 170 °C/10 h, with SBDS (sample No.b-3); and the samples calcined at (b) 400 °C; (c) 500 °C; (d) 600°C as α-Ga_2O_3 and (e) 700°C; (f) 800 °C as β-Ga_2O_3.

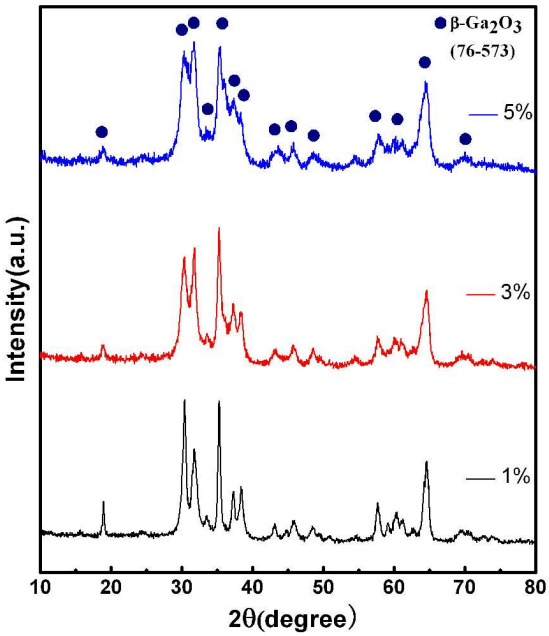

Fig.2 XRD patterns of β-Ga_2O_3 with different Ni^{2+}-doped concentration of 1%, 3% and 5%, calcined at 800 °C from GaOOH precursor (10 mol/L of Ga^{3+}) obtained at 170 °C/10 h with SBDS (sample No.b-3).

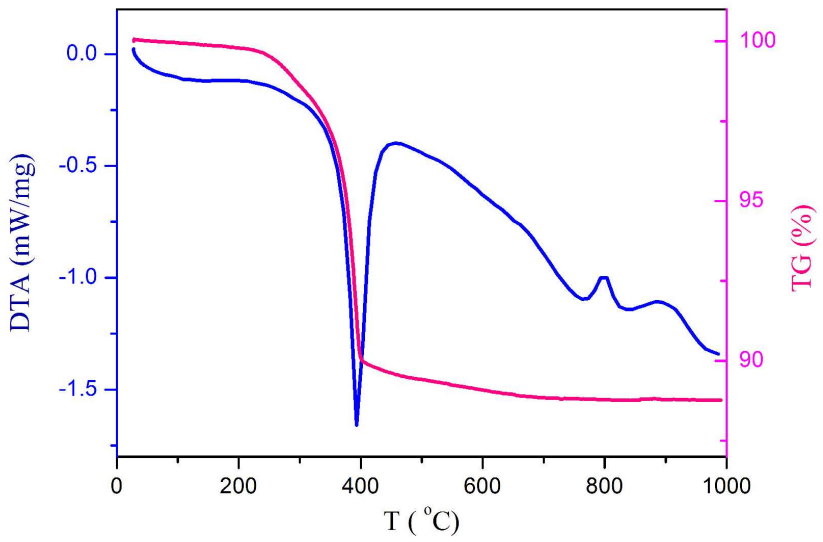

Fig.3 TG-DTA curves of GaOOH obtained at 170 °C/10 h, in 10 mol/L ionic concentration, with SBDS (sample No.b-3).

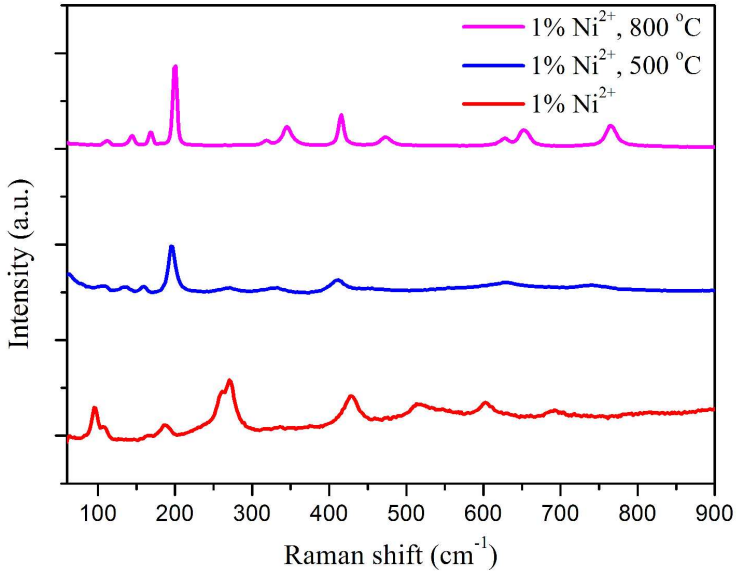

Fig.4 Raman spectra of 1% Ni^{2+}-doped GaOOH, α-Ga_2O_3 and β-Ga_2O_3 (sample No. d-1).

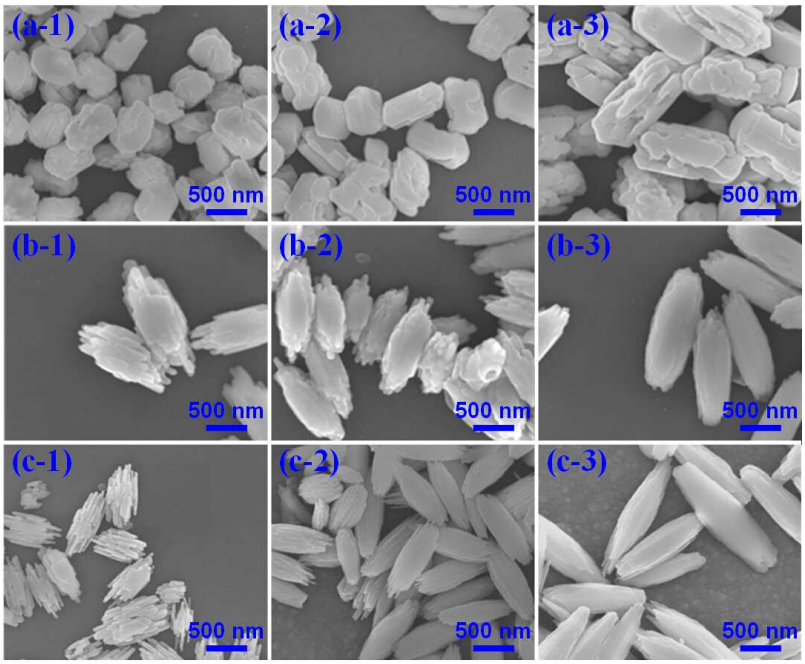

Fig.5 Typical SEM images of GaOOH under different experimental conditions: (x-1), (x-2),2 (x-3){x=a,b,c} are in 0.8, 5, 10 mol/L of Ga^{3+}, respectively. (a-1)~(a-3) are under 170 °C/10 h, without SDBS; (b-1)~(b-3) are under 170 °C/10 h, with SDBS; and (c-1)~(c-3) are under 150 °C/10 h, with SDBS. All the scale bar is 500nm.

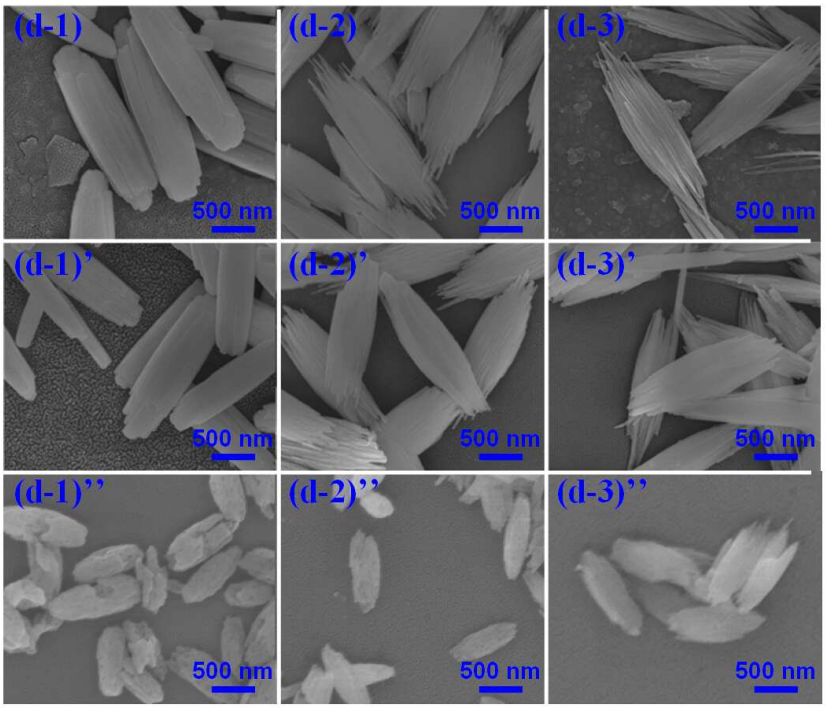

Fig.6 Typical SEM images of (d-1)~(d-3): GaOOH with 1%, 3%, 5% Ni^{2+}-doped, respectively (170 °C/10h, with SDBS, 10 mol/L of Ga^{3+}); (d-1)'~(d-3)': 600°C calcination products as α-Ga_2O_3 from (d-1)~(d-3), respectively; and (d-1)''~(d-3)'':800 °C calcination products as β-Ga_2O_3 from (d-1)~(d-3), respectively. All the scale bar is 500nm.

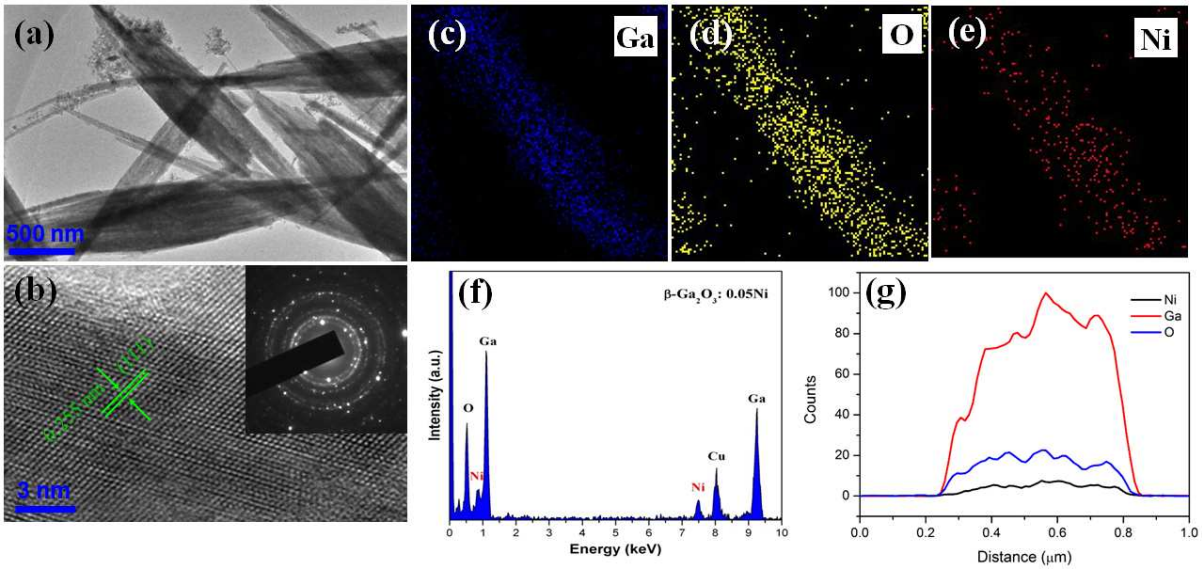

Fig.7 (a) TEM, (b) HR-TEM and SAED images (inset), (c, d, e) Ga, O and Ni EDS elemental maps, (f) EDS spectra and (g) EDS line scan profile of 5% Ni^{2+}-doped β-Ga_2O_3 obtained at 800 °C (170 °C/10 h, with SDBS, 10 mol/L of Ga^{3+}).

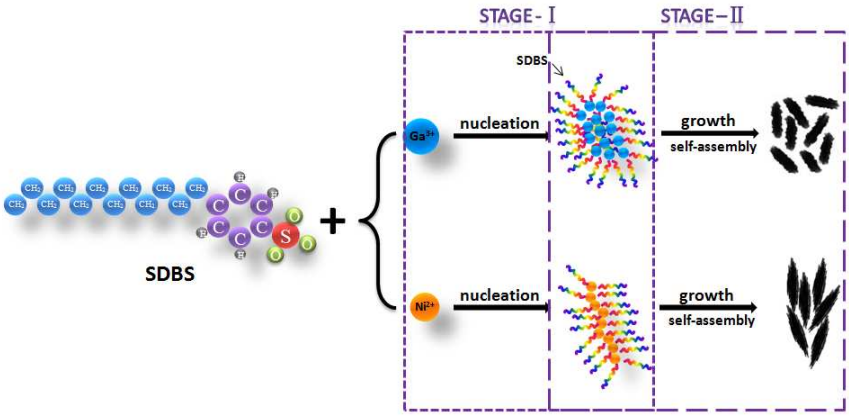

Fig.8 Growth mechanism of the GaOOH nanocrystals.

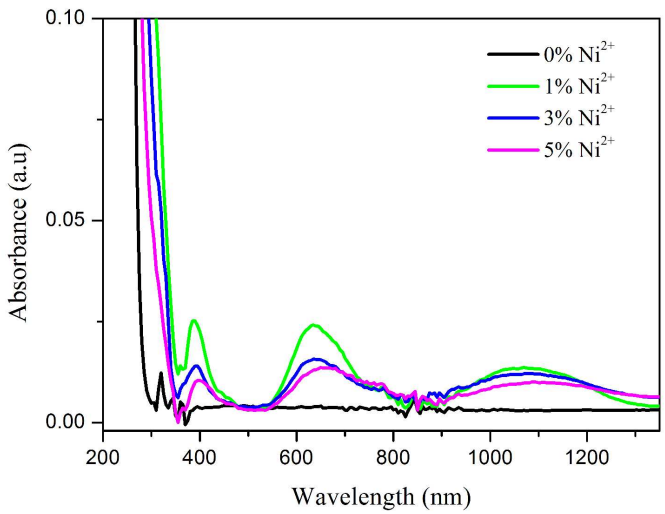

Fig.9 Diffuse reflectance absorption spectra of 0%, 1%, 3%, 5% Ni^{2+}-doped β-Ga_2O_3 obtained at 800 °C (170 °C/10 h, with SDBS, 10 mol/L of Ga^{3+}).

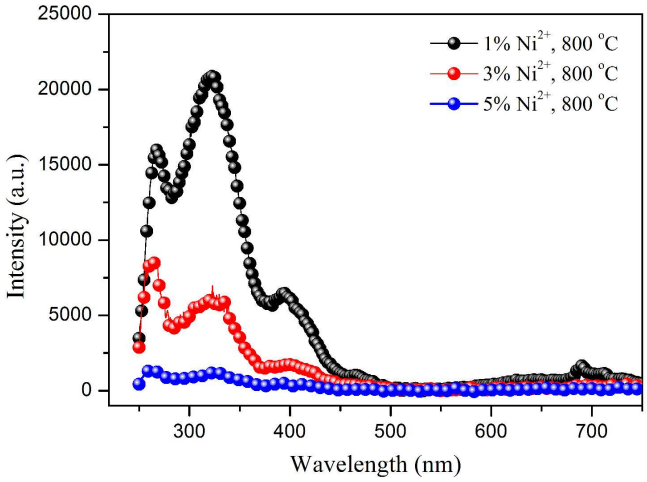

Fig.10 PL excitation spectra of different concentration of Ni^{2+} doped β-Ga_2O_3.

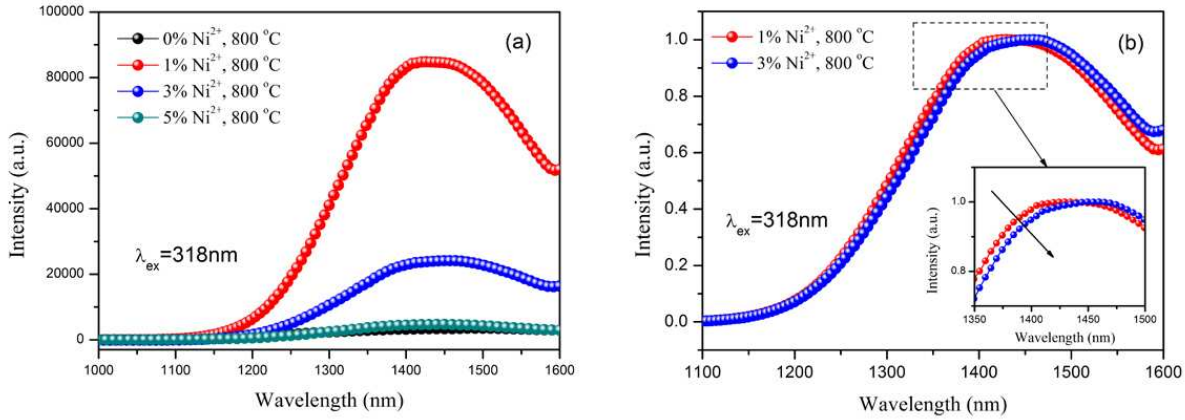

Fig.11 (a) PL emission spectra of different concentration of Ni^{2+}-doped β-Ga_2O_3 under 318nm excitation, and (b) normalized PL emission spectra of 1%, 3% Ni^{2+}-doped β-Ga_2O_3 (inset is the amplified PL spectra).

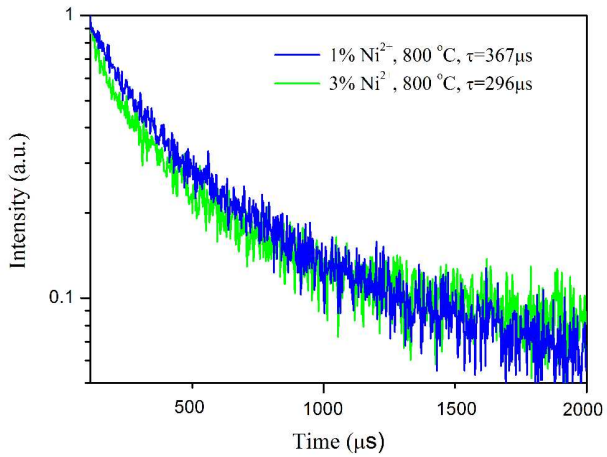

Fig.12 PL decay curve of 1%, 3% Ni^{2+}-doped β-Ga_2O_3.

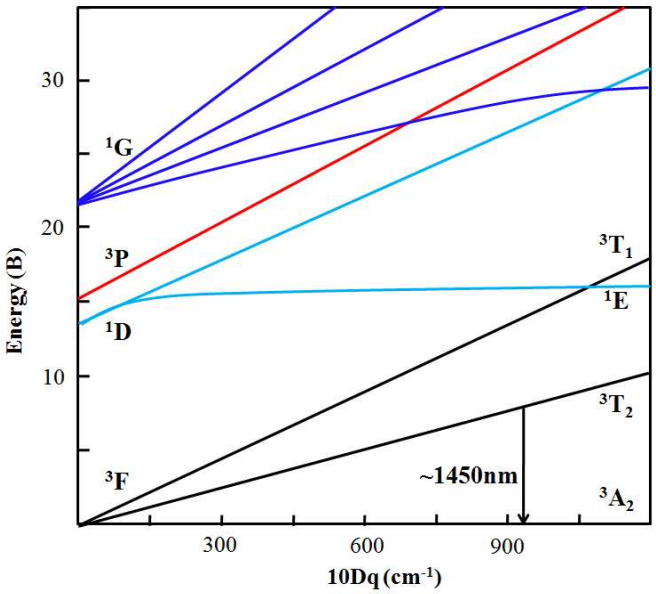

Fig.13 Tanabe–Sugano (TS) diagram of Ni^{2+}-doped β-Ga_2O_3.

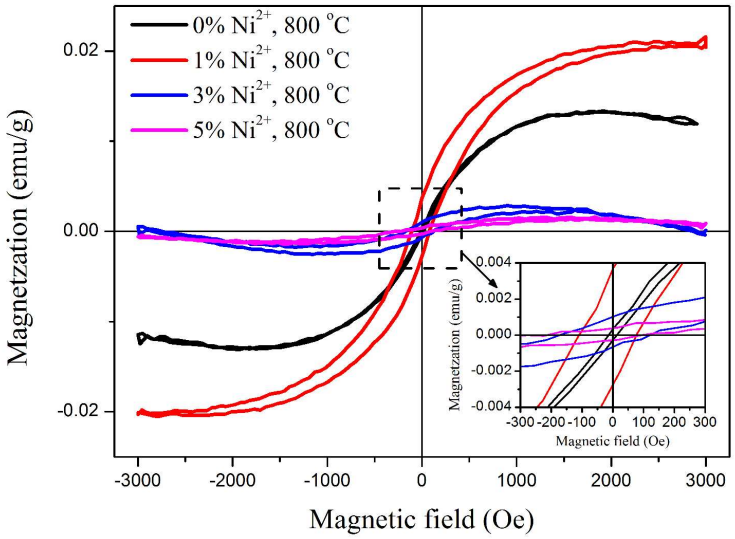

Fig.14 M–H curves of 0%, 1%, 3%, 5% Ni^{2+}-doped β-Ga_2O_3 (inset is the amplified M–H curves of 0%, 1%, 3%, 5% Ni^{2+}-doped β-Ga_2O_3).

Graphical Abstract

Broadband near-infrared emission (1200~1600 nm) and ferromagnetic properties was detected from single phase Ni^{2+}-doped β-Ga_2O_3 nanocrystals via mediated phase-controlled synthesis. The realization of optical-magnetic bifunctional nanocrystals is meaningful for the application in high-accuracy communications, bio-labels, etc.